Electronic Supplementary Information (ESI)

Topotactic synthesis of high-entropy sulfide nanosheets as efficient pre-catalysts for water oxidation

Min Guo,[†,a] Pengfeng Li,[†,a] Anran Wang,[a] Jiale Wang,[a] Jinyue Chen,[a] Fengcai Lei,[a] Pin Hao,[a] Xu Sun,[*,b] Junfeng Xie[*,a] and Bo Tang[*,a]

a College of Chemistry, Chemical Engineering and Materials Science, Key Laboratory of Molecular and Nano Probes (Ministry of Education), Collaborative Innovation Center of Functionalized Probes for Chemical Imaging in Universities of Shandong, Institute of Molecular and Nano Science, Shandong Normal University, Jinan, Shandong, 250014, P. R. China. E-mail: xiejf@sdnu.edu.cn; tangb@sdnu.edu.cn

b Key Laboratory of Interfacial Reaction & Sensing Analysis in Universities of Shandong, School of Chemistry and Chemical Engineering, University of Jinan, Jinan 250022, Shandong, P. R. China. Email: chm_sunx@ujn.edu.cn

† These authors contributed equally to this work.

S1. Experimental Section

S1.1 Chemicals

The chemicals were purchased from Sinopharm Chemical Reagent Co., Ltd. and used as received without further purification.

S1.2 Synthesis of layered metal hydroxide (LMH) precursors

Taking the synthesis of the high-entropy LMH (HE-LMH) as an example, $Ni(NO_3)_2 \cdot 6H_2O$ (0.004 mmol), $Co(NO_3)_2 \cdot 6H_2O$ (0.004 mmol), $Fe(NO_3)_3 \cdot 9H_2O$ (0.003 mmol), $Cu(NO_3)_2 \cdot 3H_2O$ (0.004 mmol), $Cr(NO_3)_3 \cdot 9H_2O$ (0.003 mmol) were dissolved in 20 mL deionized water under magnetic stirring. Next, Na_2CO_3 (0.016 mol) and NaOH (0.039 mol) were dissolved in 20 mL deionized water to form another solution. Then, the solution of Na_2CO_3 and NaOH was subsequently injected into the solution of metal salts. Afterwards, the solution was stirred for 30 min to obtain a uniform colloidal suspension, and the colloidal solution was transferred into a 50 mL Teflon-lined stainless-steel autoclave. The autoclave was sealed and maintained at 80 ºC for 48 h, and then allowed to cool to room temperature. The product was rinsed with distilled water and ethanol for several times and finally dried under vacuum overnight. For the synthesis of the quaternary, ternary, binary and unary LMH, the metal salts were modified as following.

NiCoFeCr LMH: The cationic metal salts were modified as 0.006 mmol $Ni(NO_3)_2 \cdot 6H_2O$, 0.006 mmol $Co(NO_3)_2 \cdot 6H_2O$, 0.003 mmol $Fe(NO_3)_3 \cdot 9H_2O$, 0.003 mmol $Cr(NO_3)_3 \cdot 9H_2O$, and the other parameters remain unchanged.

NiCoCr LMH: The cationic metal salts were modified as 0.006 mmol $Ni(NO_3)_2 \cdot 6H_2O$, 0.006 mmol $Co(NO_3)_2 \cdot 6H_2O$, 0.006 mmol $Cr(NO_3)_3 \cdot 9H_2O$, and the other parameters remain unchanged.

NiCo LMH: The cationic metal salts were modified as 0.009 mmol $Ni(NO_3)_2 \cdot 6H_2O$, 0.009 mmol $Co(NO_3)_2 \cdot 6H_2O$, and the other parameters remain unchanged.

Ni LMH: The cationic metal salts were modified as 0.018 mmol $Ni(NO_3)_2 \cdot 6H_2O$, and the other parameters remain unchanged.

S1.3 Fabrication of the sulfurized LMHs

Taking the synthesis of high-entropy metal sulfide derived from LMH (HE-LMH-S) as an example, 50 mg HE-LMH was dispersed in 40 mL deionized water by magnetic stirring, then 0.376 g thioacetamide (TAA; 5 mmol) was added and dissolved by vigorous stirring for 30 min. The mixture was then transferred into a 50 mL Teflon-lined stainless-steel autoclave, and maintained at 100 ºC for 12 h. After that, the reaction system was allowed to cool to room temperature naturally. The as-obtained powdery product was washed with deionized water and ethanol for several times, and then dried in vacuum at 40 ºC. Controlling samples of quaternary metal sulfide ($NiCoFeCrS_x$), ternary metal sulfide ($NiCoCrS_x$), binary metal sulfide ($NiCoS_x$), and single metal sulfide (NiS_x) were prepared using the same method.

1.4 Structural characterizations

The X-ray diffraction (XRD) was performed on a Philips X'Pert Pro Super diffractometer with Cu Kα radiation ($\lambda = 1.54178$ Å). The scanning electron microscopy (SEM) images were taken on a JEOL JSM-6700F SEM. The transmission electron microscopy (TEM) was carried out on a JEM-2100F field emission electron microscope at an acceleration voltage of 200 kV. The high-resolution TEM (HRTEM), high-angle annular dark-field scanning transmission electron microscopy (HAADF-STEM) and corresponding elemental mapping analyses were performed on a Thermo Fischer Talos F200X TEM. The atomic ratio of metals was determined by inductively coupled plasma optical emission spectrum (ICP-OES) on a Perkin Elmer Optima 7300DV ICP emission spectroscope. The X-ray photoelectron spectroscopy (XPS) analyses were performed on a VGESCALAB MKII X-ray photoelectron spectrometer with an excitation source of Mg Kα = 1253.6 eV, and the resolution level was lower than 1 atom%.

1.5 Electrocatalytic study

All the electrochemical measurements were performed in a three-electrode system linked with an electrochemical workstation (Ivium Vertex. C. EIS). All potentials were calibrated to a reversible hydrogen electrode (RHE) according to the Nernst equation and the data were presented without iR correction. Typically, 4 mg of catalyst and 50 μL Nafion solution (Sigma Aldrich, 5 wt%) were dispersed in 1 mL water-isopropanol

mixed solution (volume ratio of 3:1) by sonicating for at least 30 min to form a homogeneous ink. Then 5 μL of the dispersion (containing 20 μg of catalyst) was loaded onto a glassy carbon electrode with 3 mm diameter, resulting in a catalyst loading of 0.285 mg cm^{-2}. The as-prepared catalyst film was allowed to be dried at room temperature. The cyclic voltammetry (CV) and linear sweep voltammetry (LSV) with a scan rate of 2 mV s^{-1} were conducted in O$_2$-purged 1 M KOH solution. A Hg/HgO electrode was used as the reference electrode, a platinum gauze electrode (2 cm × 2 cm, 60 mesh) was used as the counter electrode, and the glassy carbon electrodes loaded with various catalysts were served as the working electrodes. The electrochemical impedance spectroscopy (EIS) measurements were operated in the same configuration at 1.55 V vs. RHE from 10^{-2}-10^5 Hz.

## 2. Supplementary physical and electrochemical characterizations
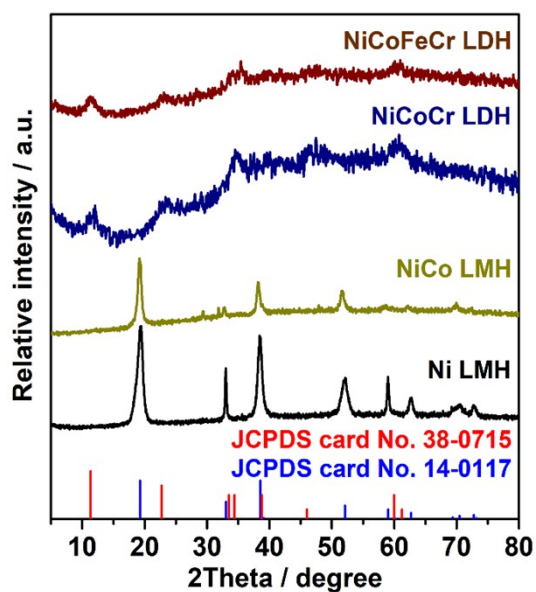
Fig. S1 XRD patterns of the metal hydroxide precursors. Standard cards: α-Ni(OH)$_2$ (JCPDS Card No: 38-0715); β-Ni(OH)$_2$ (JCPDS Card No: 14-0117).
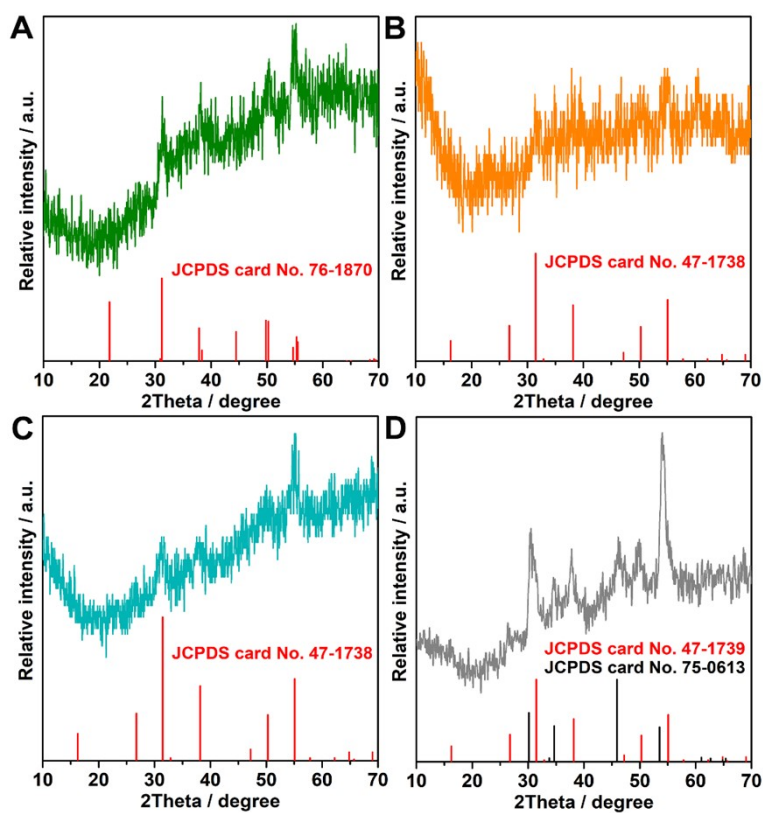

Fig. S2 (A-D) XRD patterns of quaternary NiCoFeCrS$_x$, ternary NiCoCrS$_x$, binary NiCoS$_x$ and unary NiS$_x$.

Of note, multi-metal feature is the prerequisite for the topotactic transformation process. When reducing the number of elements, phase separation may take place. For example, nickel sulfides usually exist in the form of Ni_3S_2, Ni_3S_4, NiS and NiS_2, while the $Ni_2S_2 \cdot xH_2O$ structure cannot be formed and stabilized owing to the low structural stability. Hence, owing to the lattice mismatch between $M_2S_2 \cdot xH_2O$ and the above Ni sulfides, topotactic transformation from unary Ni hydroxide to $Ni_2S_2 \cdot xH_2O$ cannot be realized. As a result, phase separation with the emerging Ni_3S_4 (JCPDS card No. 47-1739) and NiS (JCPDS card No. 75-0613) was resulted.
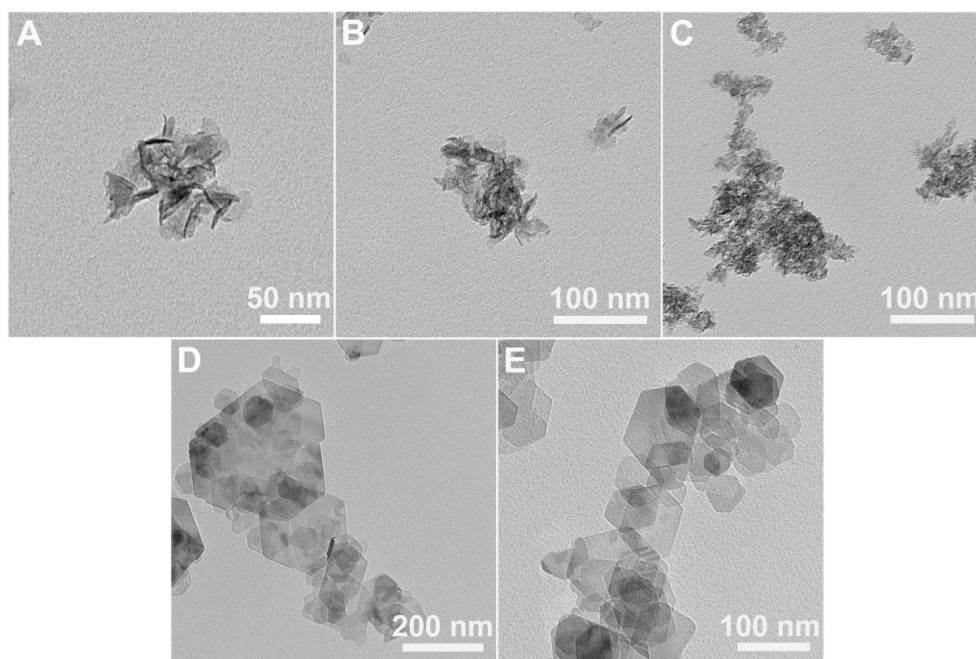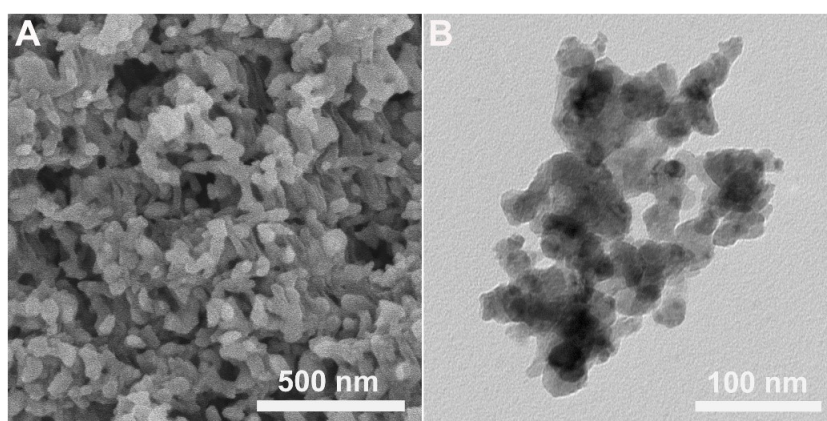

Fig. S3 TEM images of (A) NiCoFeCuCr LMH (HE-LMH), (B) NiCoFeCr LMH, (C) NiCoCr LMH, (D) NiCo LMH and (E) Ni LMH.
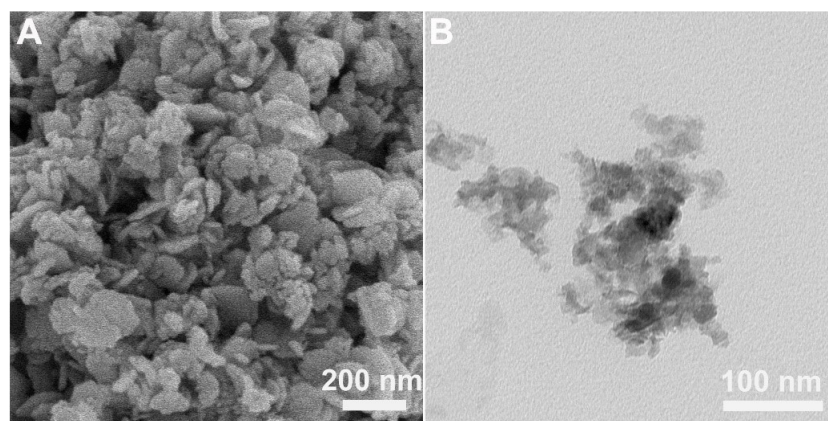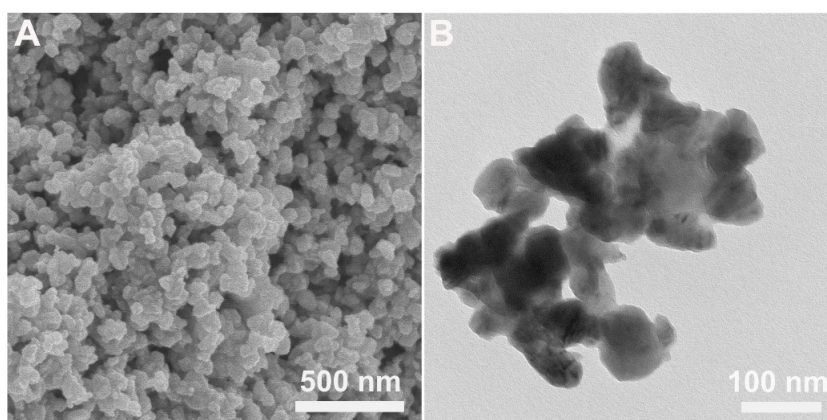

Fig. S4 (A-B) SEM and TEM images of $NiCoFeCrS_x$.
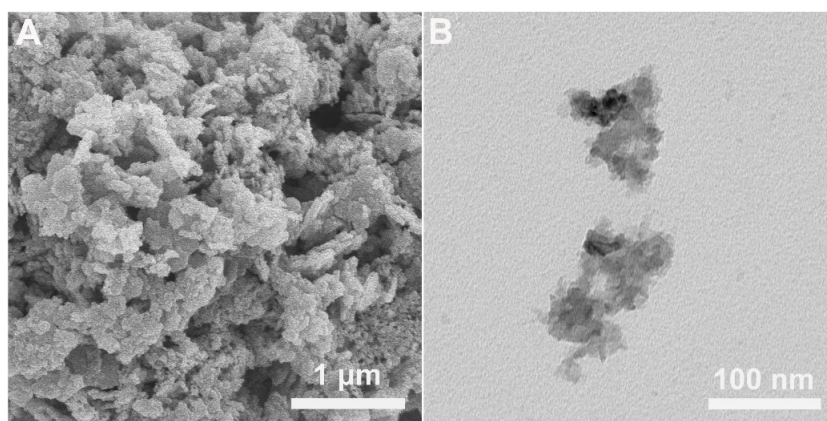
Fig. S5 (A-B) SEM and TEM images of NiCoCrS$_x$.

Fig. S6 (A-B) SEM and TEM images of NiCoS$_x$.

Fig. S7 (A-B) SEM and TEM images of NiS$_x$.

Table S1 Comparison of the OER activity.

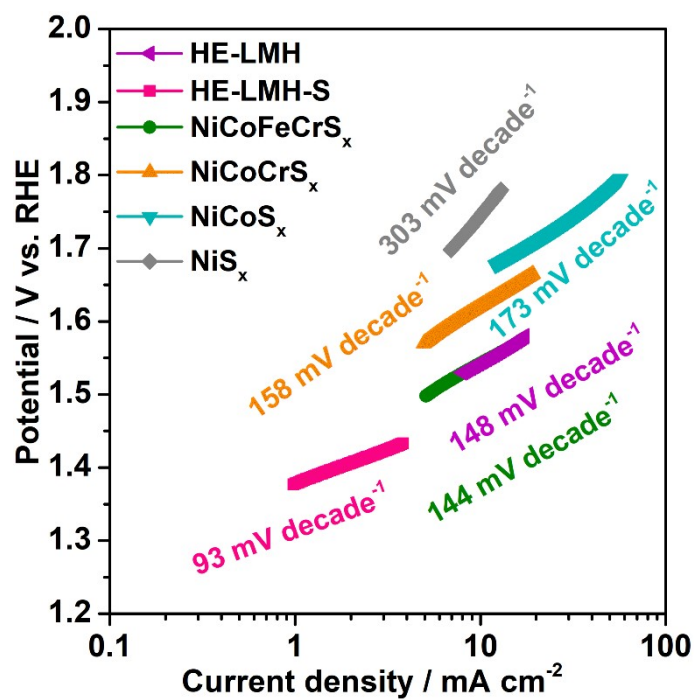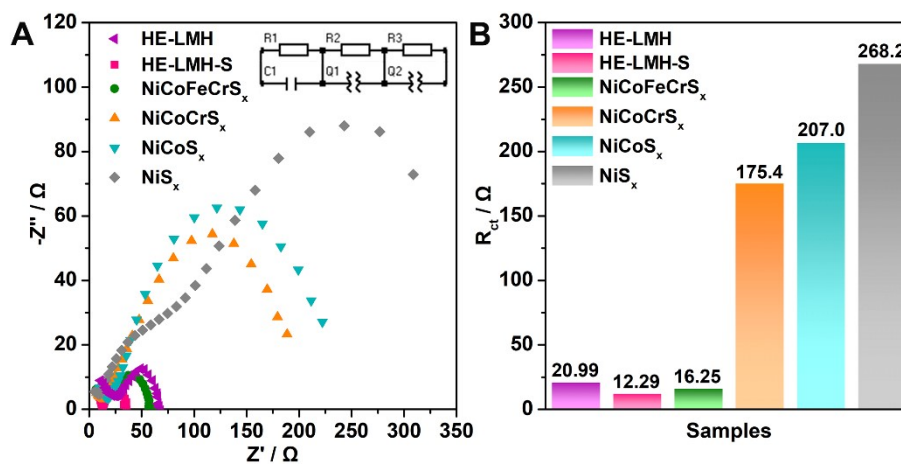|	j_{geo}@1.7 V vs. RHE [mA cm^{-2}]	η_{10} [mV]	j_{Cdl}@$\eta_{400\ mV}$ [A F^{-1}]	Ref.
HE-LMH	55.8	318	482.4	this work
HE-LMH-S	105.2	258	725.8	this work
HE-LMH-S-ac	184.6	220	1039.0	this work
NiCoFeCrS$_x$	74.2	316	524.8	this work
NiCoCrS$_x$	30.5	395	196.4	this work
NiCoS$_x$	16.7	437	111.6	this work
NiS$_x$	7.0	519	79.8	this work
Co$_3$S$_4$@NiMoO$_4$	50.9	320	0.4	1
hydrophilic Co$_3$S$_4$	80.2	360	---	2
hydrophobic Co$_3$S$_4$	6.0	520	---	2
Zn$_{0.76}$Co$_{0.24}$S-Co$_9$S$_8$	60	330	8.7	3
Zn$_{0.76}$Co$_{0.24}$S	19	410	2.5	3
Co$_9$S$_8$	10	420	9.1	3
CoInS/NH$_2$-CNT	35	398	0.4	4
FeInS/NH$_2$-CNT	19	438	0.8	4
MnInS/NH$_2$-CNT	9.8	472	1.4	4
Co$_{1.5}$Mo$_{1.0}$S/o-MWNTs	85	311	2.2	5
MoO$_2$@MoS$_2$@Co$_9$S$_8$	20	310	0.6	6
Co$_9$S$_8$-CoSe$_2$	58	340	---	7
Co-N-C	37.6	395	1.8	8
Co-N-C/S	62.1	339	4.5	8
Co$_3$S$_4$/Co-N-C	129.1	225	11.2	8
Co$_3$S$_4$/N-C	78.1	316	5.4	8
Co-Ni$_3$S$_2$/NF	65	274	6.3	9
Co$_9$S$_8$/S-CNTs	51	311	0.8	10
CoS$_2$/CoP/CC	83	334	---	11
CoO$_x$/N-C	41.1	352	---	12
3D porous graphene film@NiCo$_2$S$_4$	65	264	---	13
NiCo$_2$S$_4$	37	310	---	13
BN-CNT@CoMoS$_{3.13}$	18	400	---	14
Co$_9$S$_8$@MoS$_2$	88	342	1.9	15
Ni$_{3.5}$Co$_{5.5}$S$_8$ NAHNs	50	333	1.0	16
Co$_9$S$_8$ HNs	23	400	0.7	16
RuO$_2$	41.8	345	---	2
IrO$_2$	42.2	320	3.0	17

Fig. S8 Tafel plots.

Fig. S9 (A) EIS data. (B) Comparison of the charge-transfer resistance (R_{ct}).
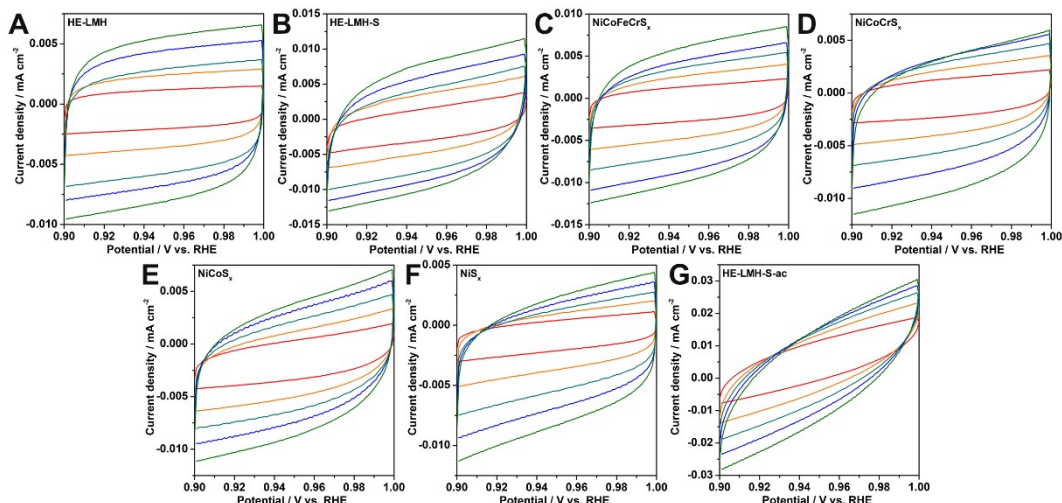
Fig. S10 (A-G) Cyclic voltammetry curves of specific samples measured in a non-redox region.

The estimation of the effective active surface area was carried out according to literature.[18, 19] Cyclic voltammetry (CV) were conducted at various scan rates (20, 40, 60, 80, 100 mV s^{-1}) in the region of 0.9-1.0 V vs. RHE where no redox reaction occurs, which can be considered as the double-layer capacitive behavior. The electrochemical double-layer capacitance (C_{dl}) can be identified from the CV curves, which is expected to be linearly proportional to the electrochemically active surface area. The C_{dl} value is estimated by plotting the Δj (j_a-j_c) at 0.95 V vs. RHE against the scan rates, where the slope is twice C_{dl}.
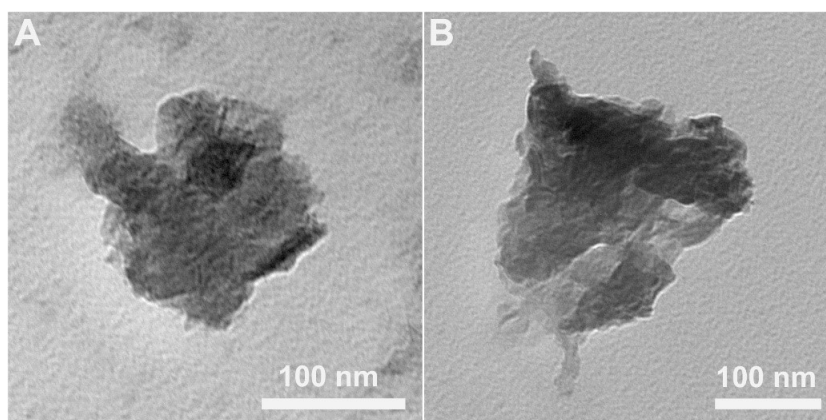
Fig. S11 (A-B) TEM images of HE-LMH-S after long-term OER catalysis.
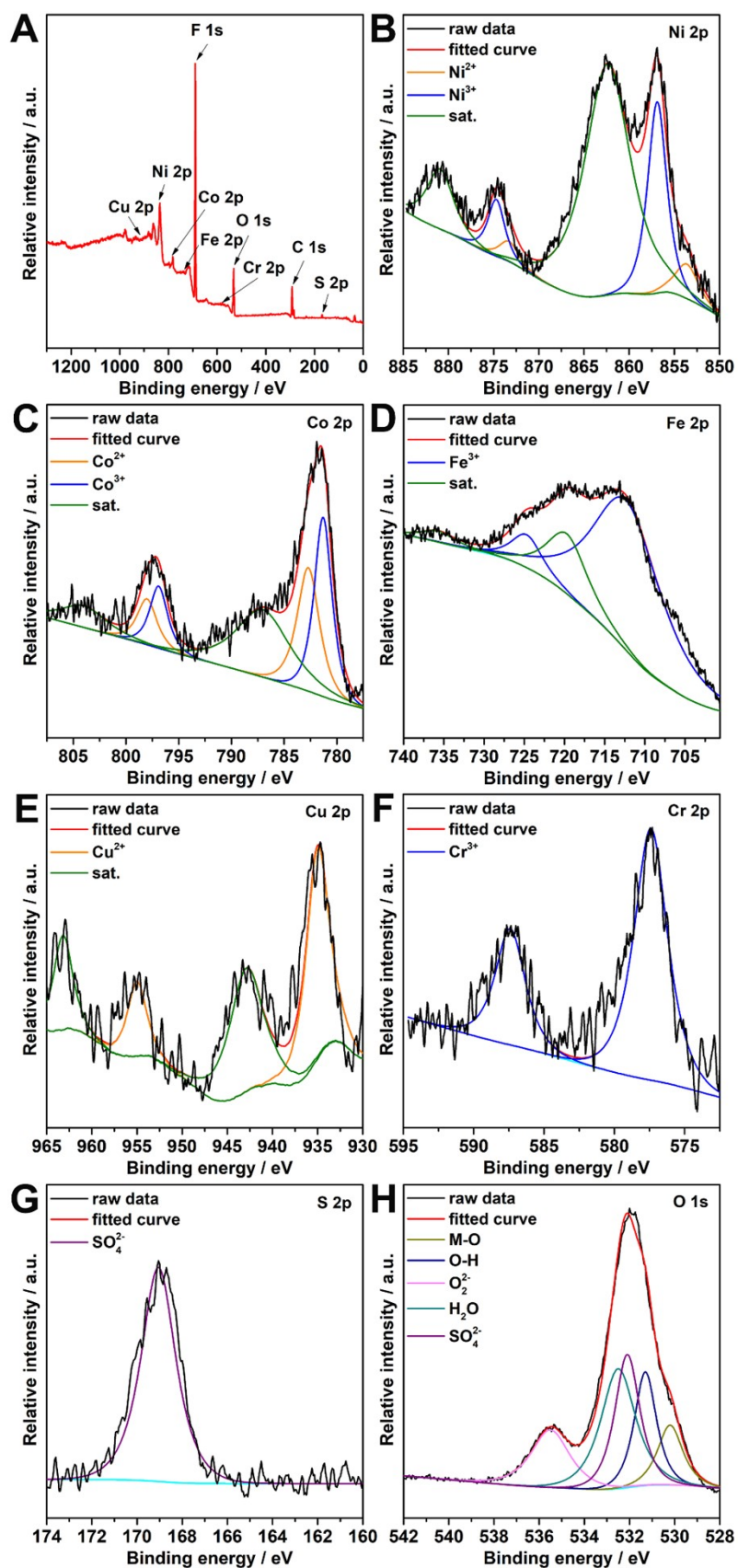
Fig. S12 (A-H) XPS spectra of HE-LMH-S after long-term OER catalysis.

Reference

1. L. Chen, G. C. Xu, G. Xu, L. Zhang and H. Ding, *Int. J. Hydrogen Energy*, 2020, **45**, 30463-30472.

2. M. Zhu, Z. Zhang, H. Zhang, H. Zhang, X. Zhang, L. Zhang and S. Wang, *J. Colloid Interface Sci.*, 2018, **509**, 522-528.

3. P. Yang, F. Kong, X. Sui, L. Zhao, Y. Qiu, H. Zhang and Z. Wang, *Int. J. Hydrogen Energy*, 2022, **47**, 8811-8819.

4. X.-L. Wang, Z. Wu, X. Wang, C. Xue, C. Liu, J. Zhang, R. Zhou, D.-S. Li and T. Wu, *Electrochim. Acta*, 2021, **376**, 138048.

5. Y. Li, L. Ji, X. Zhou, T. Li, X. Chen, X. Zhang and F. Yang, *ChemCatChem*, 2021, **13**, 3270-3274.

6. Y. Li, C. Wang, M. Cui, J. Xiong, L. Mi and S. Chen, *Appl. Surf. Sci.*, 2021, **543**, 148804.

7. S. Chakrabartty, S. Karmakar and C. R. Raj, *ACS Appl. Nano Mater.*, 2020, **3**, 11326-11334.

8. J. Xie, C. Dong, J. Li, M. Guo, Y. Zhao, L. Kang, W. Gao, F. Lei and B. Tang, *Chem. Commun.*, 2022, **58**, 6360-6363.

9. X. Wang, S. Wang, S. Chen, P. He, Y. Xu, L. Jia, D. Yang, X. He, H. Deng, B. Jia, H. Zhang and H. Liu, *Int. J. Hydrogen Energy*, 2020, **45**, 19304-19312.

10. J. Wang, H. Liu, Y. Liu, W. Wang, Q. Sun, X. Wang, X. Zhao, H. Hu and M. Wu, *Carbon*, 2019, **144**, 259-268.

11. Y. Pan, Y. Fang, H. Jin, M. Zhang, L. Wang, S. Ma, H. Zhu and M. Du, *Electrocatalysis*, 2019, **10**, 253-261.

12. H. Zhou, M. Zheng, H. Tang, B. Xu, Y. Tang and H. Pang, *Small*, 2020, **16**, 1904252.

13. K. Qin, L. Wang, S. Wen, L. Diao, P. Liu, J. Li, L. Ma, C. Shi, C. Zhong, W. Hu, E. Liu and N. Zhao, *J. Mater. Chem. A*, 2018, **6**, 8109-8119.

14. X. Zhang, P. Ding, Y. Sun, X. Li, H. Li and J. Guo, *J. Alloys Compd.*, 2018, **731**, 403-410.

15. J. Bai, T. Meng, D. Guo, S. Wang, B. Mao and M. Cao, *ACS Appl. Mater.*

Interfaces, 2018, **10**, 1678-1689.

16. V. Ganesan, P. Ramasamy and J. Kim, *Int. J. Hydrogen Energy*, 2017, **42**, 5985-5992.

17. K. Lu, T. Gu, L. Zhang, Z. Wu, R. Wang and X. Li, *Chem. Eng. J.*, 2021, **408**, 127352.

18. M. A. Lukowski, A. S. Daniel, F. Meng, A. Forticaux, L. Li and S. Jin, *J. Am. Chem. Soc.*, 2013, **135**, 10274-10277.

19. J. Xie, J. Zhang, S. Li, F. Grote, X. Zhang, H. Zhang, R. Wang, Y. Lei, B. Pan and Y. Xie, *J. Am. Chem. Soc.*, 2013, **135**, 17881-17888.